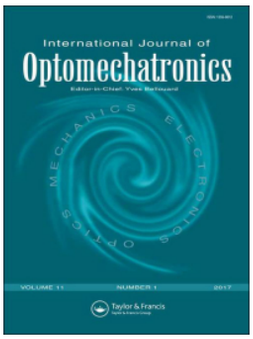

International Journal of Optomechatronics

ISSN: 1559-9612 (Print) 1559-9620 (Online) Journal homepage: www.tandfonline.com/journals/uopt20

Compact forward-viewing multimodal fluorescent and optical coherence tomograpy endomicroscopic probe

Jintaek Im, Gichan Cho & Cheol Song

To cite this article: Jintaek Im, Gichan Cho & Cheol Song (2025) Compact forward-viewing multimodal fluorescent and optical coherence tomograpy endomicroscopic probe, International Journal of Optomechatronics, 19:1, 2585610, DOI: 10.1080/15599612.2025.2585610

To link to this article: https://doi.org/10.1080/15599612.2025.2585610

Published online: 26 Nov 2025.

INTERNATIONAL JOURNAL OF OPTOMECHATRONICS
2025, VOL. 19, NO. 1, 2585610
https://doi.org/10.1080/15599612.2025.2585610

Compact forward-viewing multimodal fluorescent and optical coherence tomograpy endomicroscopic probe

Jintaek Im[a,b,c], Gichan Cho[a] and Cheol Song[a]

[a]Department of Robotics and Mechatronics Eng, DGIST, Daegu, Republic of Korea; [b]Wellman Center for Photomedicine, Massachusetts General Hospital, Boston, MA, USA; [c]Department of Dermatology, Harvard Medical School, Boston, MA, USA

ABSTRACT

We present a compact multimodal endomicroscope that enables simultaneous fluorescence (FL) and optical coherence tomography (OCT) imaging. While current endoscopy techniques are effective for wide-area and rapid inspection, there is a growing demand for real-time precise diagnostics, including detailed tissue morphology and tumor invasion depth. Histological analysis through biopsy remains the diagnostic standard but involves a time-consuming process that can delay treatment decisions. Our approach integrates two complementary imaging modalities—FL for visualizing tissue morphology and OCT for cross-sectional imaging—within a single probe compatible with standard gastrointestinal endoscopic channels. The system employs a Lissajous scanning mechanism to achieve forward-viewing, uniform illumination, and high-speed imaging. A compact imaging probe is fabricated by assembling a composite fiber, piezoelectric tube actuator, and asymmetrically attached polymer stiffener in parallel, enabling combined fluorescence and optical coherence imaging with complementary performance characteristics. Real-time image reconstruction is implemented using parallel computing to support high-throughput data processing. Imaging experiments on phantom targets and ex-vivo animal tissues confirm the system's capability to produce detailed, co-registered images of tissue morphology and structure. This technology offers a promising platform for enhancing diagnostic accuracy and enabling real-time decision-making in gastrointestinal endoscopy.

KEYWORDS

Multimodal endomicroscopy; fluorescent imaging; optical coherence tomography; piezoelectric actuator; lissajous scanning

1. Introduction

Gastrointestinal (GI) cancers, which primarily develop in the colorectum, stomach, liver, esophagus, and pancreas, represent 26% of all cancer cases globally, with approximately 3.4 million deaths estimated worldwide in 2018.[1] Among these, colorectal and stomach cancers rank highest in both incidence and mortality, contributing to 10.2% and 5.7% of all cancer cases, and 9.2% and 8.2% of cancer-related deaths, respectively. Early detection of GI cancers has been significantly advanced through endoscopic screening, supported by global health insurance systems, which has achieved a remarkable 67% reduction in cancer-related mortality compared to radiographic screening.[2] However, despite its critical role in early diagnosis, clinical endoscopy is limited by its resolution, often requiring follow-up procedures such as biopsy through endoscopic submucosal dissection and histological analysis.[3] The biopsy is performed by inserting surgical instruments, such as forceps, through a tool channel with a diameter of approximately 2.8 mm. This extended diagnostic process, spanning several days, raises the risk of cancer recurrence due to potential inaccuracies in determining cancer margin boundaries.

For simultaneous histological analysis during endoscopic procedures, confocal laser endomicroscopy (CLE) has been explored, such as developing a specialized high-resolution endoscope (eCLE) or creating a miniature imaging probe (pCLE) that can fit into the tool channel of widely used commercial endoscopes.[4] The eCLE has fewer dimensional constraints, enabling better optical performance, while the

CONTACT Cheon Song csong@dgist.ac.kr Department of Robotics and Mechatronics Eng, DGIST, Daegu, Republic of Korea.

Nomenclature

OCT	optical coherence tomography	SMF	single mode fiber
FL	fluorescence	MMF	multimode fiber
MM	multimodal	DCF	double clad fiber
GI	gastrointestinal	DCFC	double clad fiber coupler
CLE	confocal laser endomicroscopy	WDM	wavelength division multiplexor
NA	numerical aperture	GRIN	gradient-index
WD	working distance	PMT	photomultiplier tube
PTA	piezoelectric tube actuator	PD	photo detector
PIF	polyimide film		

pCLE compromises on performance but still achieves good cellular level images and market success due to its compatibility with existing systems. The representative clinically approved imaging probe is a Confocal MiniprobesTM, Cellvizio® system by Mauna Kea Technologies, which carries the CE number (CE0459) and the Food and Drug Administration (FDA) approval.[5] The typical pCLE procedure involves the intravenous delivery of Fluorescein, an FDA-approved contrast agent, immediately prior to the endoscopy. This allows it to bind to the extracellular matrix of the tissue epithelium, allowing the observation of the histological morphology of the tissue surface.[6] Since only a single working channel is available in the endoscope, the procedure is typically performed by first using the imaging probe to inspect the lesion, followed by removal of the probe and reinsertion of the resection or biopsy instruments to sample the targeted tissue. The entire process is continuously monitored through the endoscope, making this workflow feasible. However, most pCLE systems have a working distance (WD) of approximately 50 μm, limiting detection to cases where only the surface of GI cancer is visible. For a more comprehensive diagnosis, it is advantageous to simultaneously image the depth of cancer invasion.

Multimodal (MM) endomicroscopy has been developed to integrate multiple existing optical techniques into a single system. Two main visualization approaches are commonly employed: (1) high-resolution en-face imaging, such as confocal fluorescence,[7] two-photon fluorescence,[8] and non-linear microscopies,[9] and (2) deep-tissue imaging techniques, such as photoacoustic[10] or optical coherence tomography (OCT),[11] for evaluating cancer penetration. High-resolution en-face imaging techniques offer submicron lateral resolution with tens-of-micrometers axial resolution, while OCT provides micrometer-scale cross-sectional imaging with ~1 mm penetration depth, albeit with resolution-depth tradeoffs. When they share optical paths, compromises are necessary, as the high numerical aperture (NA) required for high-resolution microscopy's lateral resolution conflict with the low NAs needed for OCT's deeper tissue penetration. Marques et al.[12] addressed this tradeoff by integrating separate confocal fluorescence and OCT systems into a single probe, enabling simultaneous multimodal imaging but encountering challenges with image co-registration and dimensional alignment. Makhlouf et al.[13] used relay optics with a fiber bundle catheter, integrating confocal fluorescence and spectral-domain OCT via free-space optics. However, cross-talk between fiber cores and limited coupling efficiency into the fiber bundle compromised performance. Further advancements using fiber optics, such as double-clad fibers (DCFs) for co-registered OCT and confocal fluorescence imaging,[14,15] show promise but compromise lateral resolution, yielding fluorescence imaging (FL) rather than true confocal resolution. Nonetheless, the MM probe effectively integrates complementary features, enabling a shared optical setup and paving the way for further development.

Most of MM probe solutions are made on side-viewing systems such as capsule endoscopy with an outer diameter of 10 mm. For the forward-viewing imaging probe, the imaging probe should be insertable through the endoscopic tool channel, which requires a diameter of 2.6 mm and a rigid length of ~12 mm. Li et al.[16] proposed forward view confocal endomicroscopies based on microelectromechanical systems (MEMS) for seamless integration. Another approach, resonant fiber scanners with piezoelectric tube actuators (PTA) can offer more compact diameters and flexible fiber optics for multimodal imaging. Xi et al.[17] proposed a 2.8 mm outer diameter PTA-based multimodal probe for two-photon and OCT imaging, employing a 0.8 NA objective lens to achieve high-resolution two-photon imaging. Consequently, OCT imaging was limited to en-face views rather than cross-sectional images. Despite its compact diameter, the probe has a rigid length exceeding 20 mm. Schulz-Hildebrandt et al.[11] developed a 1.6 mm

diameter, 13.5 mm long PTA-based probe specifically for OCT imaging by directly attaching a gradient-index (GRIN) objective lens to a fiber cantilever. Most of the previous PTA-probe design utilized spiral scanning but is susceptible to photobleaching in FL imaging.[18]

We present a compact Lissajous-scanning multimodal (MM) endomicroscope for simultaneous FL and OCT imaging. Lissajous scanning ensures uniform illumination and high-speed imaging and has been widely applied in confocal forward-viewing endomicroscopy.[19,20] It uses two sinusoidal waveforms of different frequencies to form a rectangular field, often with both axes driven by resonant scanners.[21] Depending on the greatest common divisor (GCD) of the frequencies, the pattern is repeating or non-repeating; particularly for endomicroscopy, integer GCDs are selected for stable imaging, with the GCD defining the repetition time and thus the imaging speed.[22] Compared to raster or spiral scanning, Lissajous scanning offers faster sampling and distributes illumination more evenly, reducing photobleaching.[18] To enable Lissajous-scanned MM imaging, we designed a fiber cantilever compatible with both 488 nm FL and 1310 nm OCT, featuring a balanced NA and an asymmetrically attached polyimide film (PIF) to separate the mechanical resonant frequencies. We previously demonstrated that PIF is a promising candidate for an asymmetric stiffener due to its low cost, ease of fabrication, and adequate stiffness, attributed to frequency separation, while minimally impacting fiber deflection.[23] The asymmetric MM fiber cantilever is integrated into a PTA, which improves compactness and enlarges the scanning area through a lever mechanism.[20] The assembly is then enclosed by an optical window that protects the optics while providing a common-path reference for OCT. Real-time image reconstruction is achieved using parallel computing. Phantom and ex-vivo tissue imaging validate the system's FL and OCT imaging capability. Beyond GI endoscopy, the proposed compact imaging probe offers potential for a variety of clinical applications, particularly imaging in confined spaces and minimally invasive microsurgery. When combined with the depth-resolving capability and phase-sensitivity of OCT, it could facilitate autofocusing,[24] endoscopic visual serving,[25] precise tool positioning,[26–28] and force-measuring surgical tool,[29] thereby advancing both basic research and clinical translation.

2. System design

2.1. System configuration

A schematic of the proposed multimodal endomicroscopic system is shown in Figure 1. The system is divided into three main sections: optical, electrical, and the imaging probe. The optical section includes a 1310 nm swept-source laser (SS-laser, benchtop engine, AXSUN) operating at a 200 kHz sweep rate for OCT imaging, and a 488 nm continuous wave laser (CW laser, OBIS 488, Coherent, Inc) for fluorescence (FL) imaging. An optical circulator (CIR), constructed with single-mode fiber (SMF), directs the OCT illumination (port 2) and detection (port 3) pathways, while a photodetector (PD, PDB480C-AC, Thorlabs) collects the OCT fringe data. A wavelength division multiplexer (WDM), also made with SMF, combines the 1310 nm and 488 nm illumination lights, directing the mixed light to a double-clad fiber coupler (DCFC). After the WDM, the 1310 nm channel showed ~95% throughput, while 488 nm was ~50%, consistent with previous reports.[30] The DCFC transmits both OCT and FL illumination light through the single-mode core, which is then connected to a DCF (DCF13, Thorlabs) with a 9 µm single-mode core and 105 µm multimode cladding. Reflected light from the sample is delivered to both the FL and the OCT detection units. For FL signal collection, two focusing lenses and a 520 nm emission filter (FBH520-10, Thorlabs) selectively capture the FL emission from the dye (fluorescein), which is detected by a photomultiplier tube (PMT, R6355, Hamamatsu).

The electrical section comprises a digitizer (ATS9360, AlazarTech) and two data acquisition boards (DAQ1 and DAQ2). The digitizer captures the OCT fringe signal from the photodetector (PD). To achieve uniform sampling in the wavenumber domain, a k-clock is connected to the external clock port, and 1280 post-trigger data points are collected using a 200 kHz swept trigger. DAQ1, a high sampling rate board (3.5 MHz, PCIe-6374, National Instruments), is used for fluorescence (FL) signal collection and for generating the driving waveform for the PZT actuator. The two-axis driving waveforms are amplified 25 times by the PZT amplifier (E-413.60, PI Ceramic) and then segmented into four electrodes, each connected to a corresponding quadrant of the PTA. The digitizer and DAQ1 are

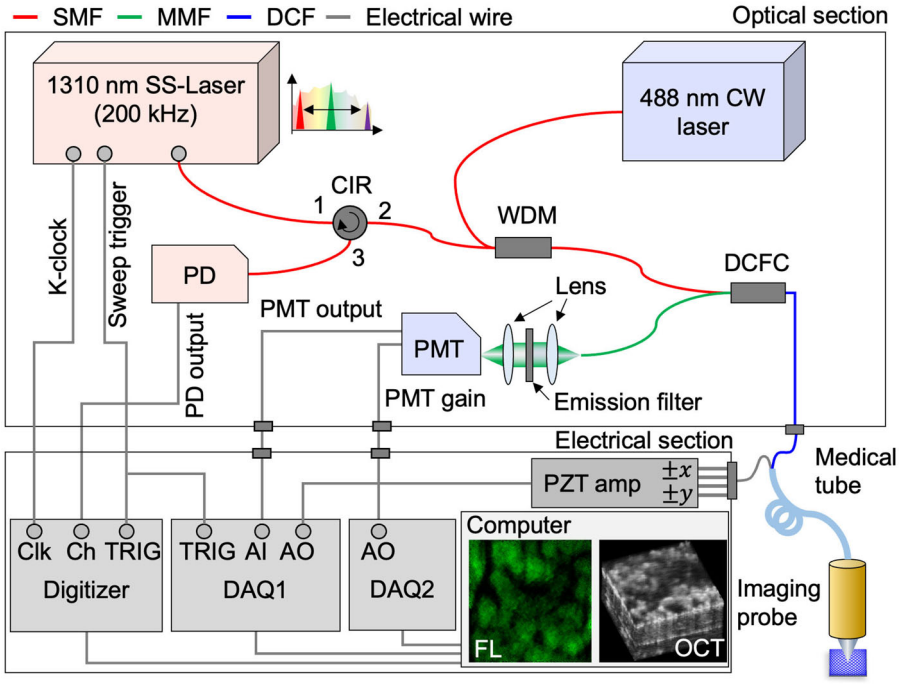

Figure 1. Configuration of a proposed multimodal endomicroscopic system. SMF: Single mode fiber, MMF: Multi mode fiber, DCF: Double clad fiber, CIR: Circulator, WDM: Wavelength division multiplexor, DCFC: Double clad fiber coupler, PD: Photo detector, PMT: Photomultiplier tube, DAQ: Data acquisition.

synchronized using the swept trigger. In contrast, DAQ2, a low sampling rate board (USB-6003, National Instruments), operates asynchronously and independently, controlling the PMT gain to adjust the sensitivity of the PMT while minimizing data transfer latency. For protection and insulation, both the output fiber and the PZT electrodes are enclosed in a Polytetrafluoroethylene (PTFE) tube with an inner diameter of 1.8 mm and an outer diameter of 2.3 mm (P0000DIW, Powertube, South Korea).

2.2. Compact imaging probe

The internal architecture of the proposed imaging probe is illustrated in Figure 2(a). We used a PTA (PI Ceramic GmbH, Germany) with customized dimensions of 10 mm in length, 1.5 mm in inner diameter, and 1.8 mm in outer diameter. Four electrodes are soldered onto the four quadrant segments of the PTA. The distal part of the PTA has a fixed anchor, while the proximal part, which includes the fiber holder, transfers load to the fiber cantilever. As a result, the fiber cantilever is anchored to the housing, while its distal end, where the GRIN lens is affixed, oscillates to acquire images. This lever mechanism significantly reduces the overall probe length, achieving an outer diameter of 2.6 mm and a rigid length of 12.2 mm. In addition, the PIF is vertically affixed to the fiber cantilever to introduce asymmetric stiffness, creating distinct resonant frequencies for the two scanning axes. The entire assembly is enclosed in a custom-designed housing, machined from non-conductive polyamide-imide (PAI) using high-precision computer numerical control (CNC) milling. An optical window at the distal end provides protection while also serving as the reference arm for common-path OCT. This common-path OCT configuration offers advantages by reducing system complexity and enhancing imaging quality through minimized material-induced dispersion.[31]

For the simultaneous FL and OCT imaging, the NA is crucial for achieving both high imaging depth and resolution. The fiber cantilever consists of a composite fiber and a GRIN rod lens (LFRL-050-025-50, GRINTECH), as shown in Figure 2(b). The composite fiber is fabricated by fuzing multiple fiber types in front of the DCF, including two coreless fibers (CLFs, FG250A, Thorlabs) and a GRIN fiber (GIF, GIF625, Thorlabs). The first CLF expands the beam from the DCF core (NA = 0.13), with its length (d_1) optimized to ensure the maximum beam diameter within the GIF does not exceed its core diameter (Φ_{GIF} = 62.5 µm). The GIF then focuses the beam with an enhanced NA of 0.275, with its length (d_2) set to position the focal point at the tip. The second CLF serves as a spacer between the

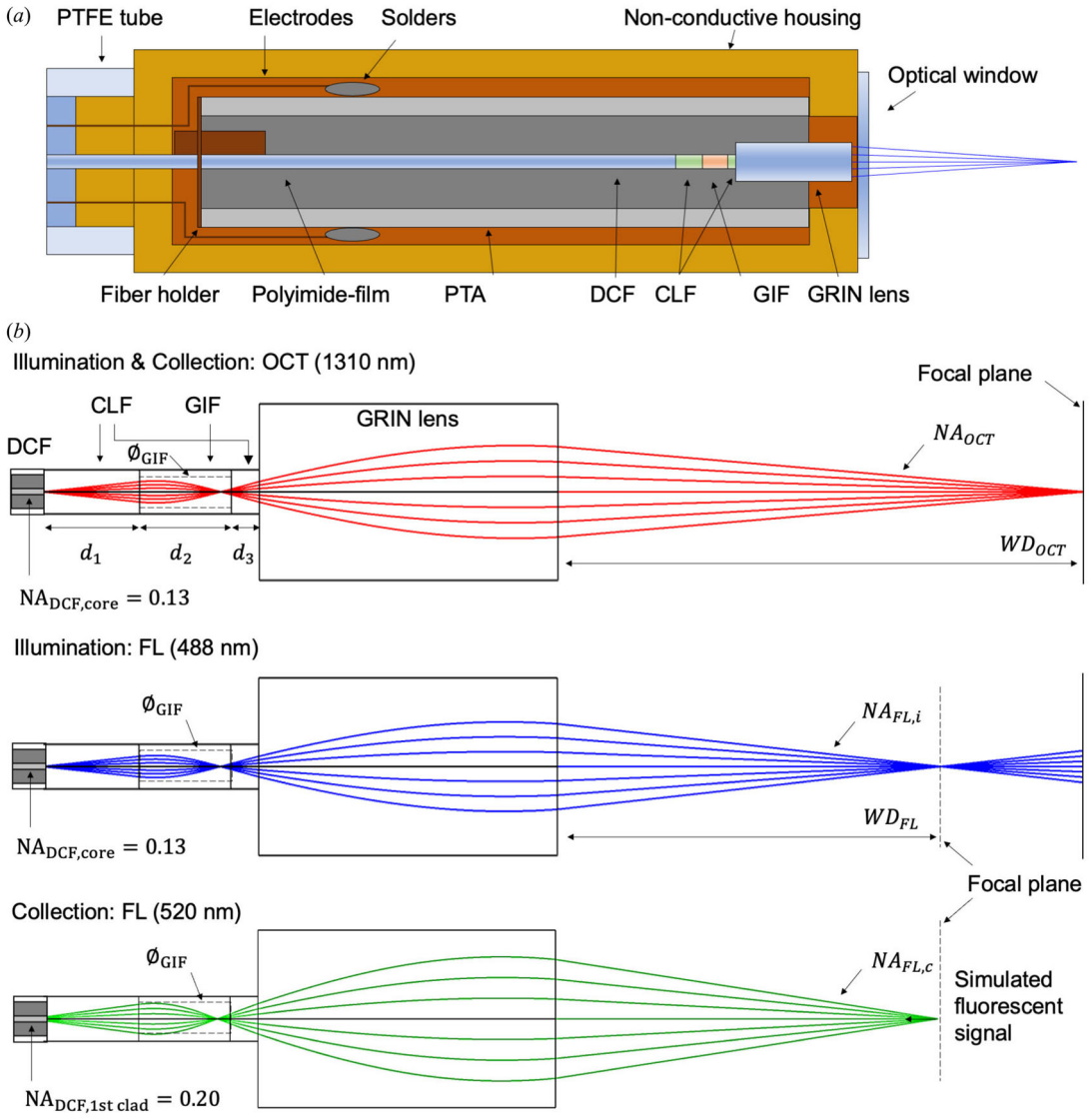

Figure 2. (a) Internal architecture of the proposed compact imaging probe. (b) The simulated beam propagation results for multimodal OCT and FL imaging. DCF: Double clad fiber, CLF: Coreless fiber, GIF: Graded-index fiber, PTFE: Polytetrafluoroethylene.

GIF and GRIN lens, where its length (d_3) significantly influences the NA and working distance of the output beam after the GRIN objective lens.

Both the illumination of OCT (1310 nm) and FL (488 nm) are delivered through the single-mode core of the DCF. Due to their wavelength difference, chromatic aberration occurs, particularly within the GRIN fiber and objective lens. It results in a separation of the output NA and working distance (WD), where the WD of the FL light (WD_{FL}) is shorter than that of OCT (WD_{OCT}). This characteristic makes OCT suitable for obtaining deeper tomographic information, while FL is well-suited for collecting fluorescent signals with low attenuation at the surface. We adjusted the WD of the OCT to 2 mm to align the focal plane centrally within our approximate 4 mm OCT imaging range. This ensures capture of the full mucosal layer and upper submucosa in most GI sites, given that mucosal thickness is typically less than a few millimeters.[32] This configuration enhances visualization of both superficial crypt and epithelial structures and deeper lamina propria features, which are critical for identifying dysplasia or early invasion. At the same time, we optimized the parameters to maximize the aperture or beam diameter to enhance the collection efficiency of the FL light. As a result, the values of d_1, d_2, and d_3 were determined to be 370 µm, 360 µm, and 100 µm, respectively. Under these conditions, the output beam parameters for OCT were $WD_{OCT} = 2$ mm and $NA_{OCT} = 0.13$, while for FL, the working distance was $WD_{FL} = 1.5$ mm, with the illumination and collection NAs being 0.17 and 0.25, respectively.

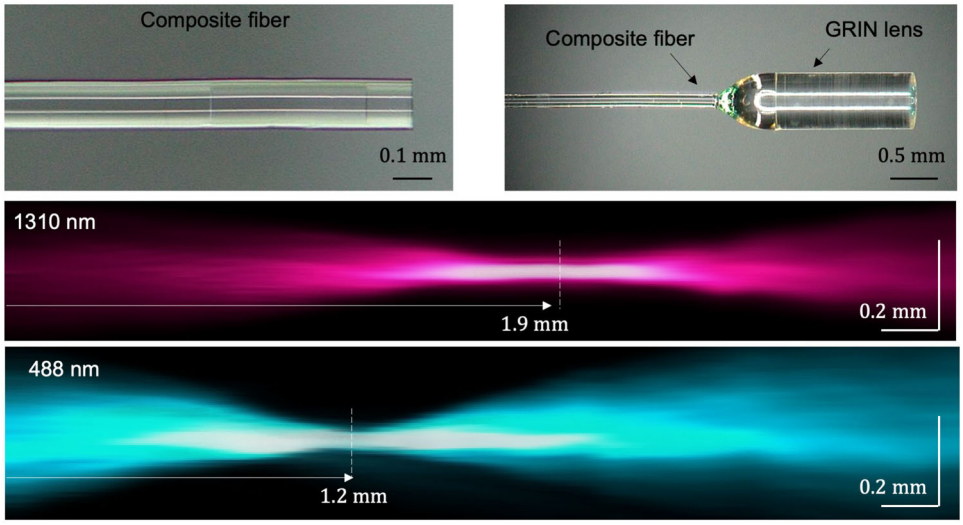

Figure 3. The implemented composite fiber and GRIN lens array for multimodal FL and OCT imaging.

The implemented composite fiber and lens arrays are shown in Figure 3. The composite fiber (DCF + CLF + GIF + CLF) was fabricated through sequential fusion splicing (S178, FITEL), with each part precisely cleaved and assembled using high-resolution digital microscopy (INSPEX3, ASH Technology Ltd) and a linear micro-stage with 1 µm resolution. Similar beam-shaping approaches have also been employed in our previous studies for various purposes.[33,34] The GRIN objective lens, which has a length of 1.15 mm and a diameter of 0.5 mm, was aligned at the fiber tip using a 5-axis stage and fixed with optical UV epoxy. The beam profile beyond the GRIN objective was obtained, where two separate focal points were observed at 1.9 mm for 1310 nm and 1.2 mm for 488 nm, respectively.

2.3. System implementation

The multimodal FL and OCT imaging probe is shown in Figure 4(a). The implemented probe has an outer diameter of 2.6 mm and a rigid length of 12.2 mm. A 2.0 mm diameter circular optical window, fabricated from a commercial 0.2 mm thick coverslip for microscopy using a high-power laser cutting system (VLS4.60, Universal Laser Systems, Inc., United States), was affixed to the probe tip using a high-strength epoxy adhesive. The probe's compatibility with a commercial GI endoscopic system (CV-260, Olympus Co. Ltd., Japan) is demonstrated in Figure 4(b). The endoscopic probe (Olympus GIF-XQ240) has an outer diameter of 9.8 mm, a length of 103 cm, and a field of view of 120°. Additionally, it features a 2.8 mm instrument channel through which the implemented imaging probe is inserted. Due to the bending angle at the channel entrance, the endomicroscopic probe requires a short rigid length of approximately 12 mm. We successfully demonstrated that the proposed compact MM probe is compatible with and insertable through the instrument channel.

The cantilever length of the proposed probe is approximately 10 mm, with a typical resonance frequency of around 1 kHz. However, due to the added mass of the GRIN lens, both the resonant frequency and bandwidth are significantly reduced, resulting in 255 Hz and 305 Hz for the x- and y-axes, respectively. The long axis of the PI film corresponds to the y-axis, which has higher stiffness, leading to a higher resonant frequency. Due to the high Q-factor, a frequency difference of only 50 Hz was sufficient to prevent cross-talk between the two axes. The scanning patterns for the two operational wavelengths, 488 nm and 1310 nm, are shown in Figure 4(d), where clean Lissajous trajectories are observed. Since both wavelengths share the same optical path, their x- and y-axis scanning trajectories are identical, while their focal depths differ by approximately 0.5 mm due to wavelength-dependent focusing. As shown in Figure 4(e), the entire system—including the optical section, electrical section, computer, and imaging probe—is integrated onto a medical cart, maximizing system portability and ensuring compatibility with conventional GI endoscopic systems.

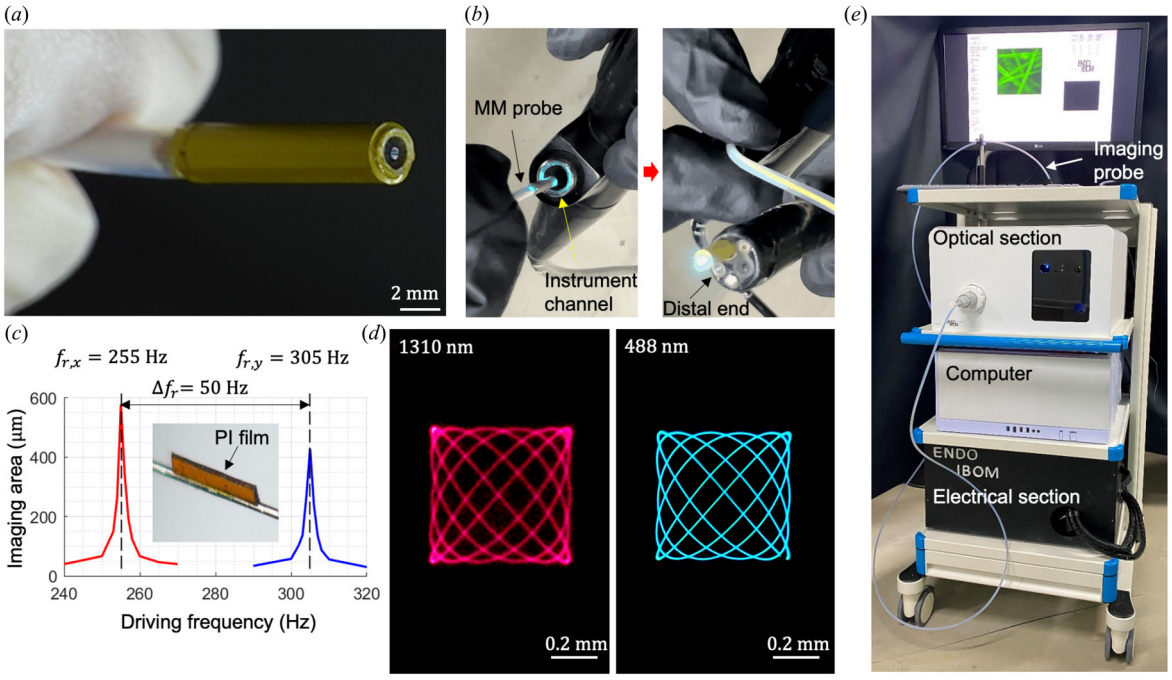

Figure 4. The implemented multimodal endomicroscopic system: (a) Packaged imaging probe. (b) Compatibility test with a commercial GI endoscopic instrument channel. (c) Frequency response of the imaging cantilever. (d) Scanning pattern for two operational wavelengths. (e) Complete system mounted on a medical cart.

2.4. Real-time image reconstruction

The cantilever length of the proposed probe is approximately 10 mm, with a typical resonance frequency The schematic of the signal processing for multimodal (MM) FL and OCT imaging is shown in Figure 5. The process is primarily divided into two sections: one for the computations handled by the central processing unit (CPU) as the host and the other for parallel processing carried out by the device, graphical processing unit (GPU). First, the waveform analog output and data acquisition performed on the host are sampled based on a swept trigger (200 kHz), with 500 samples per batch sent out, resulting in an update rate of 400 Hz. The batch size is determined by the Lissajous sampling parameters and the GPU's processing load capacity. The PZT driving waveform consists of two sinusoidal waves, and the driving frequency is chosen near the scanner's resonant frequency to achieve the highest Lissajous sampling density and repetition rate. In our case, at 255 Hz and 305 Hz, Lissajous patterns with lobe numbers of 51 and 61 for each axis are obtained at a rate of 5 Hz, which is directly used as the driving frequency. As a result, the two waveforms repeat every 5 Hz, and after transmitting 80 batches, or 40,000 samples, the Lissajous pattern repeats.

For each batch, the PMT signal for the FL image consists of 1×500 data points, while the OCT spectrum signal contains 1280×500 data points, both of which are transmitted to the host. To process these signals, data is first transferred from the CPU to the GPU. The FL data undergoes a normalization process followed by contrast adjustment, resulting in a 1×500 signal. For the OCT data, more complex processing is required: the 1280 samples are zero-padded to 2048, followed by an FFT to extract 1024 depth profile signals, resulting in a 1024×500 dataset.

The FL and OCT signals are then mapped to pixel values, with FL stored in a 2D image array (256×256) and OCT in a 3D image array ($256 \times 256 \times 1024$). For each batch, 500 data samples are filled, and after 80 exposures, the array sampled at 5 Hz is sent back to the host. During this process, unsampled regions are filled using nearest interpolation. As a result, FL and OCT en-face and cross-sectional 2D images are displayed in real-time at a rate of 5 Hz, while the original 2D FL and 3D OCT data are stored. The entire process is implemented in a C++ environment, with a Graphical User Interface (GUI) created using Visual Studio Microsoft Foundation Class Library for execution.

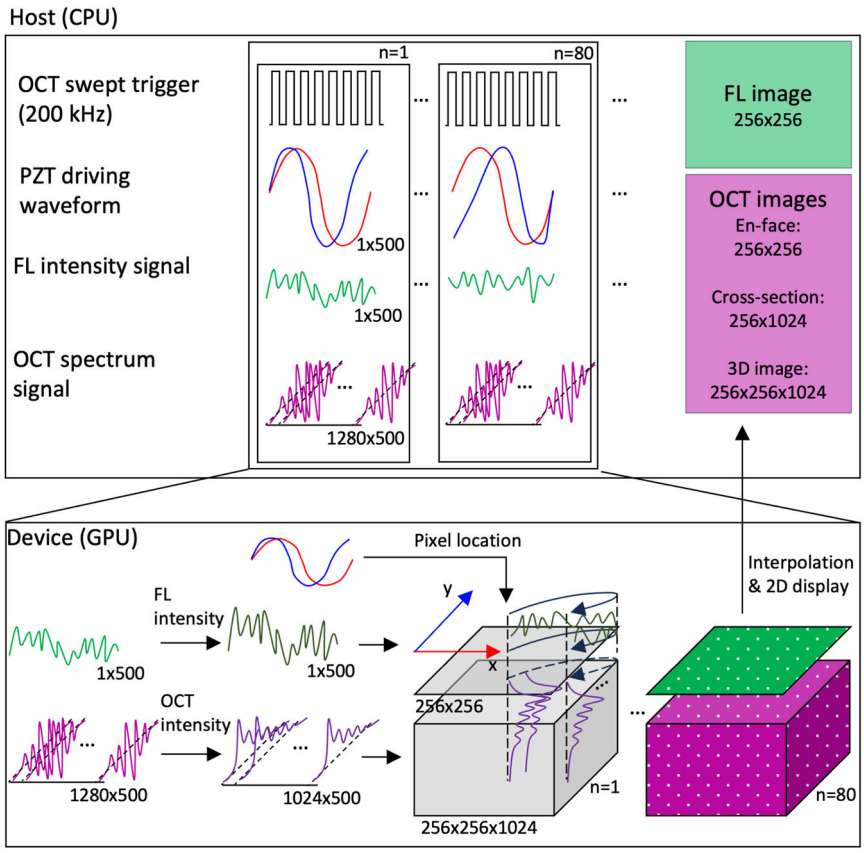

Figure 5. Schematic diagram of the signal processing workflow for multimodal FL and OCT imaging.

Given our NA and wavelengths, the theoretical diffraction-limited resolutions are 2 µm × 16 µm (FL) and 5 µm × 8 µm (OCT). However, with repeating Lissajous scanning, diamond-shaped unsampled regions arise,[21] and under our parameters, the largest corresponds to ~10 pixels. Consequently, the achieved resolutions are ~12 µm × 35 µm (FL) and ~12 µm × 11 µm (OCT). The OCT axial resolution is source-dependent, with deviations mainly due to dispersion, while the other discrepancies stem from the scanning pattern. Although higher sampling density could improve resolution, it would reduce imaging speed; in this study, speed was prioritized.

3. Results and discussion

3.1. Imaging results: phantom test

For OCT imaging using the implemented multimodal imaging probe, stacking ten layers of cellophane tape were used as a phantom, as shown in Figure 6(a). This phantom was chosen to serve as a structured, multi-layered sample to evaluate the imaging performance and depth-resolving capability of the probe. During the imaging process, the probe was moved across the phantom by a linear stage while continuously capturing OCT images. To improve the saving process, we enabled the selection of desired vertical and horizontal layers through the GUI, and generated 2D images (both en-face and cross-sectional) by averaging five layers centered on the selected layer, which were saved in real time. The acquired cross-sectional OCT images were stitched together, forming a detailed composite representation of the phantom's depth structure, as shown in Figure 6(b). This stitched cross-sectional image clearly delineates the boundaries of each individual layer, demonstrating the system's ability to resolve fine structural details with high fidelity. Furthermore, en-face OCT images were extracted at different depths, providing additional confirmation of the layered structure. As shown in the insets (b1) and (b2), the en-face images effectively distinguish each layer, reinforcing the imaging probe's capability to capture high-resolution depth information.

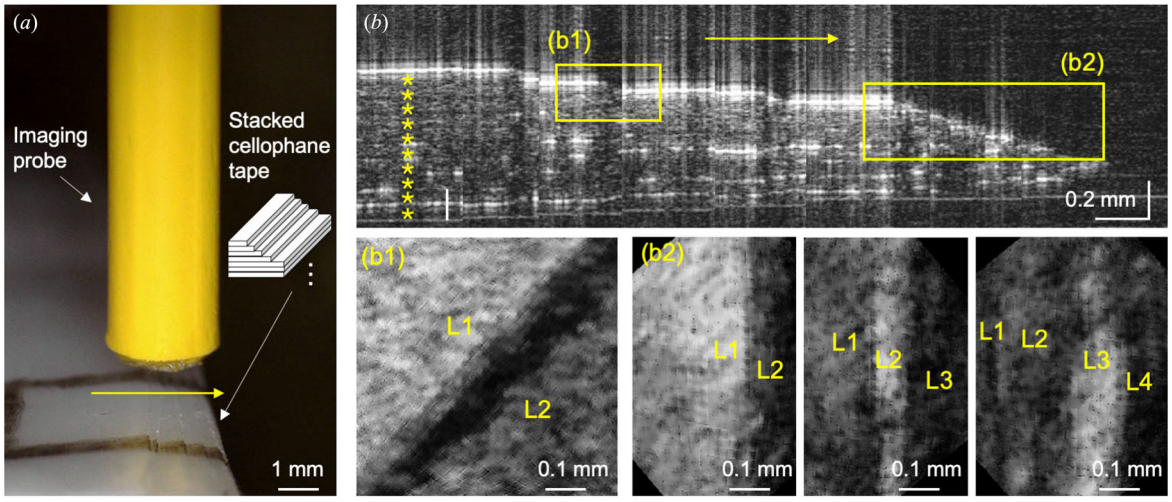

Figure 6. OCT images on the stacked cellophane tape phantom. (a) Experimental setup. (b) Stitched cross-section and several en-face images of the stacked cellophane tape phantom.

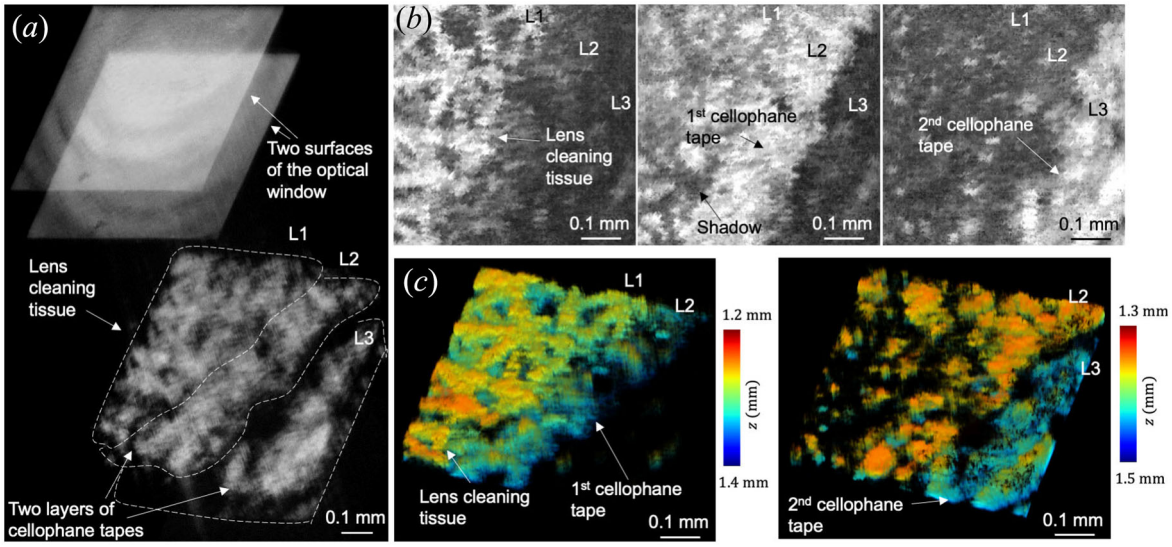

Figure 7. The multimodal imaging probe: 3D OCT images on the lens cleaning tissue phantom. (a) Post-processed 3D OCT volumetric rendering result. (b) Representative OCT en-face images at different image depth. (c) Depth-variant color-coded 3D OCT image.

The 3D OCT data can be stored in real-time, enabling post-processing for volumetric 3D rendering, as shown in Figure 7(a). Lens cleaning tissue (L1) and two layers of cellophane tape (L2 and L3) are distinctly visible, with clear separation between each layer in the en-face images (Figure 7(b)). Additionally, depth-dependent color mapping was applied for 3D rendering, as illustrated in Figure 7(c), enhancing visualization and providing a more intuitive understanding of structural details.

For multimodal FL and OCT imaging, the sample, consisting of lens cleaning tissue soaked with fluorescein (20 mg/mL) and stacked cellophane tape, was used, as shown in Figure 8. The OCT cross-sectional image clearly distinguish both the tissue layers and the cellophane tape (Figure 8(b)), while the en-face OCT image provided a detailed visualization of the combined morphology of the cleaning tissue (Figure 8(c)). In contrast, the FL image effectively isolated the single tissue layer emitting a fluorescent signal, offering enhanced structural contrast (Figure 8(d)). These features were further accentuated in the stitched images (Figure 8(e) and (f)), demonstrating the capability of the proposed imaging probe to concurrently capture both fluorescent signals and cross-sectional morphologies with high spatial resolution.

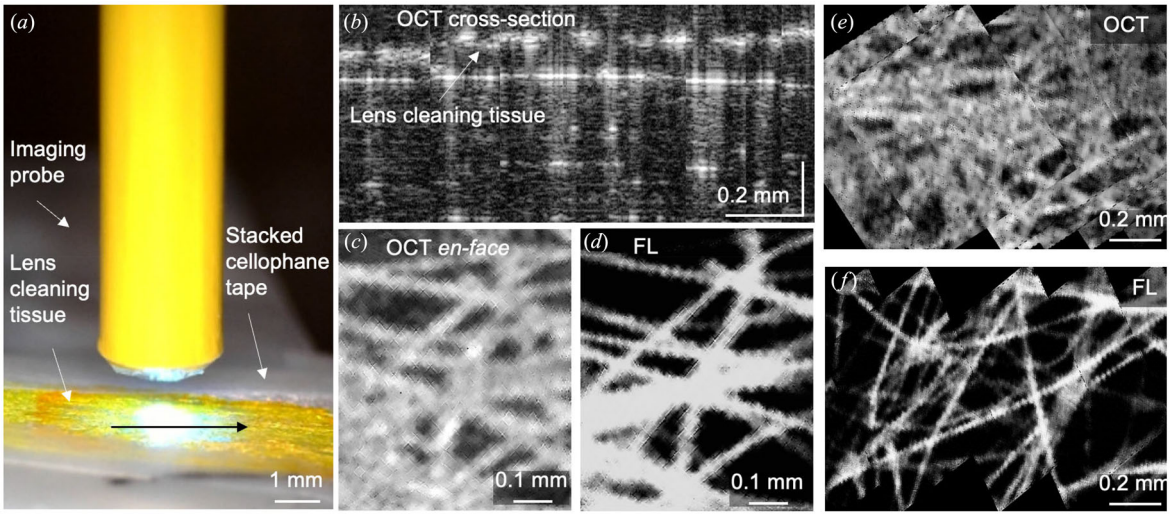

Figure 8. The multimodal imaging probe: FL and OCT images on lens cleaning tissue phantom. (a) Experimental setup. (b) Stitched OCT cross-section image. (c) OCT en-face and (d) FL images of the lens cleaning tissue at the top layer. (e) Stitched OCT en-face and (d) FL images.

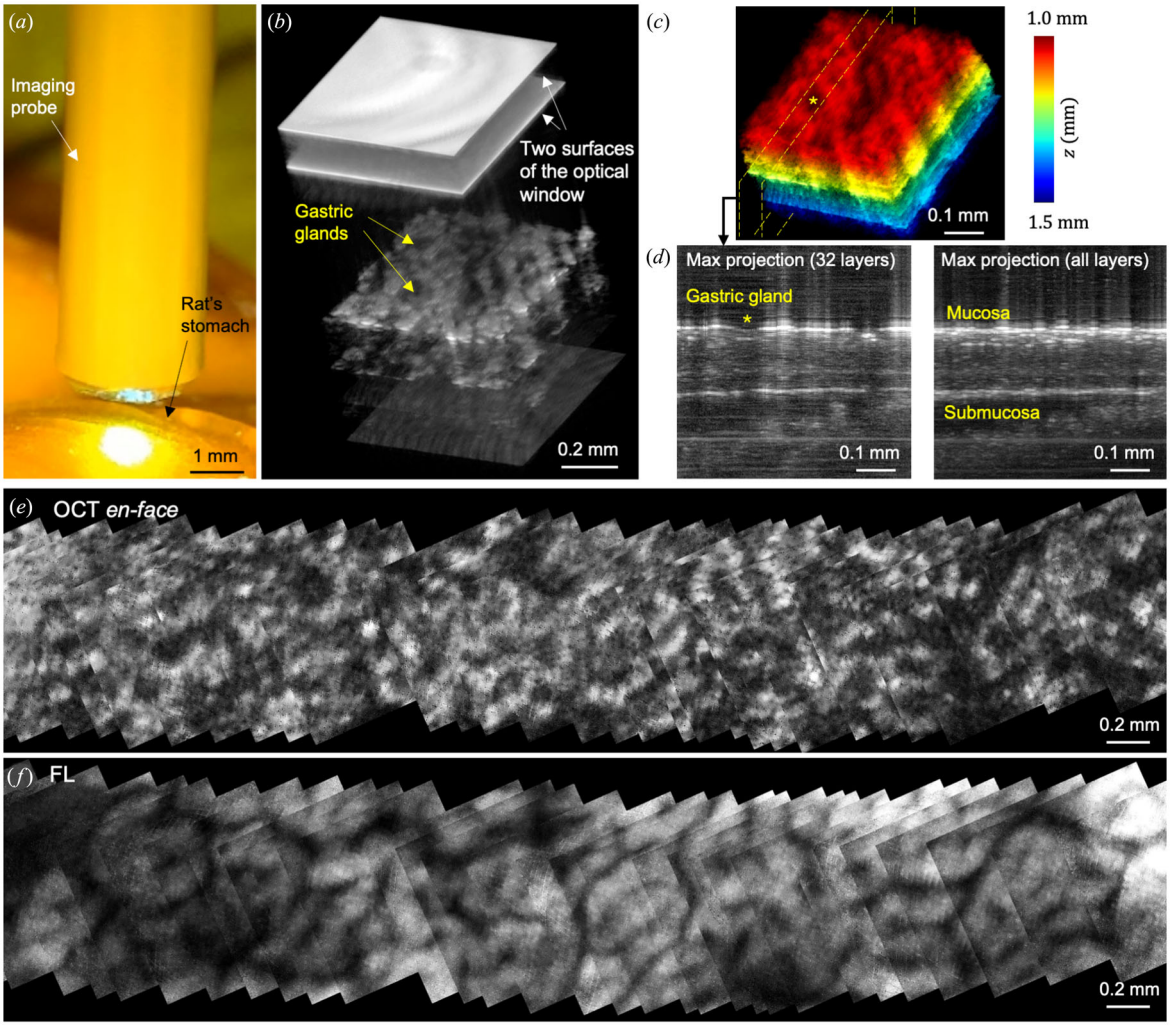

Figure 9. Panoramic and 3D reconstructed rat's stomach images by the multimodal FL and OCT imaging probe. (a) Experimental setup. (b) Post-processed 3D OCT volumetric and (c) color-coded rendering results. (d) Max-intensity projected OCT cross-section images. (e) Panoramic OCT en-face and (f) FL images.

3.2. Imaging results: biological sample

As an ex-vivo biological sample, rat stomach is extracted and used as a sample, as shown in Figure 9(a). Alterations in gastric gland morphology are well-recognized markers of malignant transformation in early gastric metaplastic and neoplastic processes, making gland imaging highly relevant for early detection.[35] Moreover, the morphology of gastric glands in rodents has been shown to closely resemble that of human gastric gland organization.[36] All surgical procedures were conducted in accordance with ethical guidelines and were approved by the Animal Experiment Ethics Committee of Daegu Gyeongbuk Institute of Science and Technology (approval no. DGIST-IACUC-21042801-0001). Every step was carefully performed to minimize discomfort and distress. The rat was anesthetized using inhaled isoflurane to ensure a pain-free procedure. Additionally, a fluorescein solution (20 mg/mL) was administered via tail vein injection at a volume of 1 mL to facilitate FL imaging. The stomach was excised within approximately 30 minutes after sacrificing the rat. Following excision, the stomach was transected and opened, and the imaging probe was mounted on a micro-stage and maneuvered to acquire both OCT and FL images.

The post-processed 3D OCT image provided a detailed visualization of the gastric gland structure, revealing its three-dimensional morphology (Figure 9(b)). To enhance visualization and improve interpretability, a region of interest (ROI) was selected, enabling a color-coded representation that facilitates the identification of specific structural features (Figure 9(c)). Given that OCT data is inherently volumetric, image projection (e.g., maximum-intensity projection) along the x- or y-axis (Figure 9(d)) allowed for improved differentiation between the mucosa and submucosa layers, offering a clearer anatomical distinction. Furthermore, various image reconstruction techniques were applied to enhance the spatial characterization of the sample, including panoramic OCT imaging (Figure 9(e)) and FL imaging (Figure 9(f)). These imaging modalities provided complementary insights, enabling the simultaneous acquisition of surface morphology, fluorescence contrast, cross-sectional structure, and volumetric data. Both real-time imaging and post-processed analyses were achieved using the proposed multimodal endomicroscopic system, demonstrating its capability for comprehensive structural and functional visualization of biological tissues.

4. Conclusion

In this study, we developed a compact Lissajous-scanning multimodal FL-OCT imaging probe. To optimize imaging performance, we engineered a fiber cantilever that balances both NA and WD for 488 nm and 1310 nm by combining multiple fiber types with a distal GRIN rod lens. The integration of GRIN-attached asymmetric imaging fiber enables a high Q-factor and resonant frequency separation, facilitating efficient Lissajous scanning. This scanning mechanism ensures uniform illumination and high-speed image acquisition, making the system particularly suitable for forward-viewing endomicroscopy applications. The MM fiber cantilever is integrated within a tube actuator in a parallel configuration, resulting in a miniaturized probe with an outer diameter of 2.6 mm and a total length of 12.2 mm—fully compatible with standard gastrointestinal endoscopes. Real-time image reconstruction is achieved via parallel computing, enabling rapid data processing and real-time visualization. The system's imaging capabilities were validated using both phantom and ex-vivo tissue studies, successfully demonstrating simultaneous FL and OCT imaging.

The current system employs a common-path OCT configuration using an optical window as the reference plane for system simplicity. However, this design compromises imaging performance by introducing unavoidable artifacts, including multiple reference signals arising from reflections between the GRIN lens and the optical window, as well as from the proximal and distal surfaces of the window itself. Furthermore, the use of DCF permits higher-order modes that contribute additional ghost images. In future designs, we plan to incorporate a dedicated reference arm with a higher sensitivity interferometric configuration, such as a Mach–Zehnder interferometer. Additionally, applying angle polishing to the GRIN lens and introducing a tilted optical window are expected to reduce back-reflections and mitigate ghost artifacts. Moreover, designing the system for in-contact imaging with a shorter WD could further enhance performance by eliminating the air gap between the window and

the tissue, thereby reducing index mismatch. In addition, the current imaging quality was mainly limited by under sampling. This fundamental bottleneck could be mitigated by employing faster light sources, such as MHz-swept lasers, which would allow substantially higher sampling rates and more flexible scanning parameters without compromising image quality.

Beyond visualizing superficial tissue layers, the system has strong potential for real-time monitoring of tumor invasion depth, which is critical for assessing cancer progression. When combined with surgical instruments, this imaging probe could support precise intraoperative guidance by helping determine the optimal biopsy depth and delineate tumor margins more accurately. Its compact form factor, high-speed scanning, and real-time imaging capabilities make it a promising tool for advanced ex-vivo clinical diagnostics and image-guided interventions, with the potential to significantly improve outcomes in early cancer detection and minimally invasive surgery.

Disclosure statement

No potential conflicts of interest was reported by the author(s).

Funding

The authors gratefully acknowledge the National Research Foundation of Korea (NRF) grant funded by the Korea government (MSIT) (RS-2024-0033398), the Technology Innovation Program (20023168), Development of clinician collaborative robot platform technology for 3 types of pain interventional procedures based on cross drug handler and instrument modules) funded by the Ministry of Trade of Trade, Industry &Energy(MOTIE, Korea), and the Basic Science Research Program through the National Research Foundation of Korea(NRF) funded by the Ministry of Education(RS-2024-00405663).

References

[1] Arnold, M.; Abnet, C. C.; Neale, R. E.; Vignat, J.; Giovannucci, E. L.; McGlynn, K. A.; Bray, F. Global Burden of 5 Major Types of Gastrointestinal Cancer. *Gastroenterol* **2020**, *159*, 335–349.e15. DOI: 10.1053/j.gastro.2020.02.068.

[2] Hamashima, C.; Shabana, M.; Okada, K.; Okamoto, M.; Osaki, Y. Mortality Reduction from Gastric Cancer by Endoscopic and Radiographic Screening. *Cancer Sci.* **2015**, *106*, 1744–1749. DOI: 10.1111/cas.12829.

[3] Buchner, A. M.; Shahid, M. W.; Heckman, M. G.; Krishna, M.; Ghabril, M.; Hasan, M.; Crook, J. E.; Gomez, V.; Raimondo, M.; Woodward, T.; et al. Comparison of Probe-Based Confocal Laser Endomicroscopy with Virtual Chromoendoscopy for Classification of Colon Polyps. *Gastroenterol.* **2010**, *138*, 834–842. DOI: 10.1053/j.gastro.2009.10.053.

[4] Chauhan, S. S.; Abu Dayyeh, B. K.; Bhat, Y. M.; Gottlieb, K. T.; Hwang, J. H.; Komanduri, S.; Konda, V.; Lo, S. K.; Manfredi, M. A.; Maple, J. T.; et al. Confocal Laser Endomicroscopy. *Gastrointest. Endosc* **2014**, *80*, 928–938. DOI: 10.1016/j.gie.2014.06.021.

[5] Sabbagh, C.; Fumery, M.; Yzet, C.; Chatelain, D.; Diouf, M.; Pellegrin, A.; Regimbeau, J. M. Is There Concordance between the Cellvizio System and Pathology in Determining Microscopic Inflammation at the Ileal Resection Margins in Crohn's Ileal Disease? the Cellvicrohn Study. *Surg. Open Dig. Adv.* **2023**, *11*, 100104. DOI: 10.1016/j.soda.2023.100104.

[6] Polglase, A. L.; McLaren, W. J.; Skinner, S. A.; Kiesslich, R.; Neurath, M. F.; Delaney, P. M. A Fluorescence Confocal Endomicroscope for in Vivo Microscopy of the Upper-and the Lower-gi Tract. *Gastrointest. Endosc.* **2005**, *62*, 686–695. DOI: 10.1016/j.gie.2005.05.021.

[7] Im, J.; Chang, Y.; Lee, M. H.; Do, D.; Lee, K.; Gweon, D.; Song, C. Lissajous Confocal Fluorescent Endomicroscopy with a Lever Mechanism and a Frequency Separation by an Asymmetric Polymer Tube. *Int. J. Optomechatronics* **2023**, *17*, 2238009. DOI: 10.1080/15599612.2023.2238009.

[8] Kim, D. Y.; Hwang, K.; Ahn, J.; Seo, Y.-H.; Kim, J.-B.; Lee, S.; Yoon, J.-H.; Kong, E.; Jeong, Y.; Jon, S.; et al. Lissajous Scanning Two-Photon Endomicroscope for in Vivo Tissue Imaging. *Sci. Rep.* **2019**, *9*, 3560. DOI: 10.1038/s41598-019-38762-w.

[9] Pshenay-Severin, E.; Bae, H.; Reichwald, K.; Matz, G.; Bierlich, J.; Kobelke, J.; Lorenz, A.; Schwuchow, A.; Meyer-Zedler, T.; Schmitt, M.; et al. Multimodal Nonlinear Endomicroscopic Imaging Probe Using a Double-Core Double-Clad Fiber and Focus-Combining Micro-Optical Concept. *Light. Sci. Appl.* **2021**, *10*, 207. DOI: 10.1038/s41377-021-00648-w.

[10] Liang, Y.; Fu, W.; Li, Q.; Chen, X.; Sun, H.; Wang, L.; Jin, L.; Huang, W.; Guan, B. O. Optical-Resolution Functional Gastrointestinal Photoacoustic Endoscopy Based on Optical Heterodyne Detection of Ultrasound. *Nat. Commun.* **2022**, *13*, 7604. DOI: 10.1038/s41467-022-35259-5.

[11] Schulz-Hildebrandt, H.; Pfeiffer, T.; Eixmann, T.; Lohmann, S.; Ahrens, M.; Rehra, J.; Draxinger, W.; König, P.; Huber, R.; Hüttmann, G. High-Speed Fiber Scanning Endoscope for Volumetric Multi-Megahertz Optical Coherence Tomography. *Opt. Lett.* **2018**, *43*, 4386–4389. DOI: 10.1364/OL.43.004386.

[12] Marques, M. J.; Hughes, M. R.; Vyas, K.; Thrapp, A.; Zhang, H.; Bradu, A.; Gelikonov, G.; Giataganas, P.; Payne, C. J.; Yang, G. Z.; Podoleanu, A. En-Face Optical Coherence Tomography/Fluorescence Endomicroscopy for Minimally Invasive Imaging Using a Robotic Scanner. *J. Biomed. Opt.* **2019**, *24*, 1–15. DOI: 10.1117/1.JBO.24.6.066006.

[13] Makhlouf, H.; Rouse, A. R.; Gmitro, A. F. Dual Modality Fluorescence Confocal and Spectral-Domain Optical Coherence Tomography Microendoscope. *Biomed. Opt. Express.* **2011**, *2*, 634–644. DOI: 10.1364/BOE.2.000634.

[14] Mavadia, J.; Xi, J.; Chen, Y.; Li, X. An All-Fiber-Optic Endoscopy Platform for Simultaneous Oct and Fluorescence Imaging. *Biomed. Opt. Express.* **2012**, *3*, 2851–2859. DOI: 10.1364/BOE.3.002851.

[15] Wartak, A.; Kelada, A. K.; Leon Alarcon, P. A.; Bablouzian, A. L.; Ahsen, O. O.; Gregg, A. L.; Wei, Y.; Bollavaram, K.; Sheil, C. J.; Farewell, E.; et al. Dual-Modality Optical Coherence Tomography and Fluorescence Tethered Capsule Endomicroscopy. *Biomed. Opt. Express.* **2021**, *12*, 4308–4323. DOI: 10.1364/BOE.422453.

[16] Li, G.; Li, H.; Duan, X.; Zhou, Q.; Zhou, J.; Oldham, K. R.; Wang, T. D. Visualizing Epithelial Expression in Vertical and Horizontal Planes with Dual Axes Confocal Endomicroscope Using Compact Distal Scanner. *IEEE Trans. Med. Imaging.* **2017**, *36*, 1482–1490. DOI: 10.1109/TMI.2017.2673022.

[17] Xi, J.; Chen, Y.; Zhang, Y.; Murari, K.; Li, M. J.; Li, X. Integrated Multimodal Endomicroscopy Platform for Simultaneous en Face Optical Coherence and Two-Photon Fluorescence Imaging. *Opt. Lett.* **2012**, *37*, 362–364. DOI: 10.1364/OL.37.000362.

[18] Liang, W.; Murari, K.; Zhang, Y. Y.; Chen, Y.; Li, X. D.; Li, M. J. Increased Illumination Uniformity and Reduced Photodamage Offered by the Lissajous Scanning in Fiber-Optic Two-Photon Endomicroscopy. *J. Biomed. Opt.* **2012**, *17*, 021108. DOI: 10.1117/1.JBO.17.2.021108.

[19] Hwang, K.; Seo, Y.-H.; Kim, D. Y.; Ahn, J.; Lee, S.; Han, K. H.; Lee, K.-H.; Jon, S.; Kim, P.; Yu, K. E.; et al. Handheld Endomicroscope Using a Fiber-Optic Harmonograph Enables Real-Time and in Vivo Confocal Imaging of Living Cell Morphology and Capillary Perfusion. *Microsyst. Nanoeng.* **2020**, *6*, 72. DOI: 10.1038/s41378-020-00182-6.

[20] Im, J.; Jang, E.; Song, C. Analytical Modeling and Implementation of an Imaging Cantilever with a Thermoplastic Stiffener. *IEEE/ASME Trans. Mechatron.* **2024**, *29*, 4320–4329. DOI: 10.1109/TMECH.2024.3375356.

[21] Tanguy, Q. A.; Gaiffe, O.; Passilly, N.; Cote, J. M.; Cabodevila, G.; Bargiel, S.; Lutz, P.; Xie, H.; Gorecki, C. Real-Time Lissajous Imaging with a Low-Voltage 2-Axis MEMS Scanner Based on Electrothermal Actuation. *Opt. Express.* **2020**, *28*, 8512–8527. DOI: 10.1364/OE.380690.

[22] Loewke, N. O.; Qiu, Z.; Mandella, M. J.; Ertsey, R.; Loewke, A.; Gunaydin, L. A.; Rosenthal, E. L.; Contag, C. H.; Solgaard, O. Software-Based Phase Control, Video-Rate Imaging, and Real-Time Mosaicing with a Lissajous-Scanned Confocal Microscope. *IEEE Trans. Med. Imaging.* **2020**, *39*, 1127–1137. DOI: 10.1109/TMI.2019.2942552.

[23] Im, J.; Chang, Y.; Song, C. Modified Phase-Offset-Driven Lissajous Scanning Endomicroscopy with a Polyimide-Film-Based Frequency Separator. *IEEE/ASME Trans. Mechatron.* **2022**, *27*, 4829–4839. DOI: 10.1109/TMECH.2022.3166453.

[24] Aguirre, A. D.; Sawinski, J.; Huang, S. W.; Zhou, C.; Denk, W.; Fujimoto, J. G. High Speed Optical Coherence Microscopy with Autofocus Adjustment and a Miniaturized Endoscopic Imaging Probe. *Opt. Express.* **2010**, *18*, 4222–4239. DOI: 10.1364/OE.18.004222.

[25] Xu, X.; Zhang, C.; Zhang, C.; Zuo, S. A Novel Flexible Endomicroscopic Scanning Instrument with Visual Servoing Control. *Adv. Intell. Syst.* **2024**, *6*, 2300656. DOI: 10.1002/aisy.202300656.

[26] Song, C.; Gehlbach, P. L.; Kang, J. U. Active Tremor Cancellation by a "Smart" Handheld Vitreoretinal Microsurgical Tool Using Swept Source Optical Coherence Tomography. *Opt. Express.* **2012**, *20*, 23414–23421. DOI: 10.1364/OE.20.023414.

[27] Im, J.; Song, C. Oblique Injection Depth Correction by a Two Parallel OCT Sensor Guided Handheld SMART Injector. *Biomed. Opt. Express.* **2021**, *12*, 926–939. DOI: 10.1364/BOE.410492.

[28] Im, J.; Jang, E.; Song, C. A Three-Dimensional Compliant Bowtie-Shaped Mechanical Amplifier to Magnify Coaxial Displacement in a Confined Space. In 2024 IEEE International Conference on Robotics and Automation (ICRA), Yokohama, Japan, 2024, 5884–5890. DOI: 10.1109/ICRA57147.2024.10611636.

[29] Cho, G.; Im, J.; Kwon, H.; Song, C. An Optical Interferometer-Based Force Sensor System for Enhancing Precision in Epidural Injection Procedure. In 2024 IEEE/RSJ International Conference on Intelligent Robots and Systems (IROS), Abu Dhabi, United Arab Emirates, 2024, 8393–8399. DOI: 10.1109/IROS58592.2024.10802501.

[30] Ryu, S. Y.; Choi, H. Y.; Na, J.; Choi, E. S.; Lee, B. H. Simultaneous Measurements of Optical Coherence Tomography and Fluorescence Spectroscopy Based on Double Clad Fiber. In 2009 Multimodal Biomedical Imaging IV. SPIE, San Jose, California, United States, 2009, 7171. DOI: 10.1117/12.808915.

[31] Yin, B.; Chu, K. K.; Liang, C. P.; Singh, K.; Reddy, R.; Tearney, G. J. Moct Imaging Using Depth of Focus Extension by Self-Imaging Wavefront Division in a Common-Path Fiber Optic Probe. *Opt. Express.* **2016**, *24*, 5555–5564. DOI: 10.1364/OE.24.005555.

[32] Huh, C. H.; Bhutani, M. S.; Farfán, E. B.; Bolch, W. E. Individual Variations in Mucosa and Total Wall Thickness in the Stomach and Rectum Assessed via Endoscopic Ultrasound. *Physiol. Meas.* **2003**, *24*, N15–N22. DOI: 10.1088/0967-3334/24/4/401.

[33] Im, J.; Cho, G.; Song, C. Compact Fiber-Optic Sensor for Simultaneous Force Measurement and Depth Profiling. *IEEE/ASME Trans. Mechatron.* **2025**, *20*, 1–9. DOI: 10.1109/TMECH.2025.3593334.

[34] Im, J.; Park, S.; Song, C. Handheld Motorized Injection System with Fiber-Optic Distance Sensors and Adaptive Time-Delay Controller. *Int. J. Optomechatronics* **2024**, *18*, 2299023. DOI: 10.1080/15599612.2023.2299023.

[35] Battista, S.; Ambrosio, M. R.; Limarzi, F.; Gallo, G.; Saragoni, L. Molecular Alterations in Gastric Preneoplastic Lesions and Early Gastric Cancer. *IJMS.* **2021**, *22*, 6652. DOI: 10.3390/ijms22136652.

[36] Di Natale, M. R.; Patten, L.; Molero, J. C.; Stebbing, M. J.; Hunne, B.; Wang, X.; Liu, Z.; Furness, J. B. Organisation of the Musculature of the Rat Stomach. *J. Anat.* **2022**, *240*, 711–723. DOI: 10.1111/joa.13587.